Ceramics

CrossMark

Controllable synthesis of Ho-doped In$_2$O$_3$ porous nanotubes by electrospinning and their application as an ethanol gas sensor

Haojie Duan[1], Yifang Wang[2], Shuo Li[1], Haiying Li[1], Li Liu[1,*], Liting Du[1], and Yali Cheng[1]

[1] State Key Laboratory of Superhard Materials, College of Physics, Jilin University, Changchun 130012, People's Republic of China
[2] Colleges of Mechanical Science and Engineering, Jilin University, Changchun 130012, People's Republic of China

ABSTRACT

Pure and Ho-doped In$_2$O$_3$ nanotubes (NTs) and porous nanotubes (PNTs) were successfully synthesized by conventional electrospinning process and the following calcination at different temperatures. X-ray diffractometry (XRD), thermogravimetric analysis (TGA), Raman spectrometer, energy-dispersive spectroscopy, scanning and transmission electron microscopy were carefully used to investigate the morphologies, structures and chemical compositions of these samples. Their sensing properties toward ethanol gas were studied. Compared with pure In$_2$O$_3$ NTs (response value is 17), pure In$_2$O$_3$ PNTs (response value is 20) demonstrated enhanced sensing characteristics. What's more, the response of Ho-doped In$_2$O$_3$ PNTs sensors to 100 ppm ethanol was up to 60 at 240 °C, which increased three times more than that of the pure In$_2$O$_3$ PNTs. Additionally, the minimum concentration for ethanol was 200 ppb (response value is 2). The increased gas-sensing ability was attributed not only to the hollow and porous structure, but to the Ho dopant. Furthermore, Ho-doped In$_2$O$_3$ PNTs enable sensor to discriminate between ethanol and the other gas distinctly, particularly acetone that is usually indistinguishable from ethanol. Also, by analyzing XRD, TGA and Raman spectrometer, a possible formation mechanism of porous nanotubes and sensing mechanism were put forward.

Introduction

As an important n-type transparent inorganic semiconductor functional materials, In$_2$O$_3$, because of its wide band gap, higher conductivity and fine catalytic performance, is widely employed in the areas of screen, gas sensors, ceramics and other fields. In gas sensors domain, gas sensors based on indium oxide tend to have lower resistance because of their low resistivity [1]. In recent years, reports on In$_2$O$_3$ gas sensor have gradually increased; two kinds of studies are used in material modification for the sake of further enhancing response magnitude. One is to increase the surface area to get a higher surface to

Address correspondence to E-mail: liul99@jlu.edu.cn

Springer

volume ratio to facilitate the surface-controlled process between target gas and In$_2$O$_3$ sensor. For example, Wagner et al. explored how response values of gas sensors were affected by mesoporous structure due to its modified gas diffusion performance and the formation of a sufficient depleted region, and their results indicate that mesoporous structure was essential for rapid gas response or recovery and higher response value toward target gases [2]. Moreover, Akash Katoch et al. [3] found that ZnO hollow fibers with smaller aperture made sensors much more sensitive to target gases than those with larger aperture. And, they also found that the leptodermous hollow fibers showed increased responses value to CO compared to pachypleurous hollow fibers [4]. In addition to the above methods, the other is to decorate In$_2$O$_3$ surface with precious metal (such as Ag, Pt, Au) [5–7] or doping external metals (Ni, Sn, Ti) [8–10] to improve the catalytic activity. Furthermore, rare-earth element (like La, Sm and Ce) [11–13] can serve as catalysts to increase the number of active sites or oxygen vacancies on the surface of sensing materials because of their rapid oxygen ion mobility and good catalytic performance. However, research on gas-sensing properties of Ho-doped In$_2$O$_3$ porous nanotubes (PNTs) sensor is seldom reported.

Nowadays, some methods have been developed for the synthesis of nanosized In$_2$O$_3$, including chemical vapor deposition [14], hydrothermal synthesis [15], sol–gel method [16] and electrospinning (ES) [17–19]. In this research work, we studied the controllable synthesis of Ho-doped In$_2$O$_3$ NTs and PNTs by adjusting a suitable heat-treating process via electrospinning. The method of fabricating porous structure is very simple and low cost. In addition, electrospun nanofibrous structure has large aspect ratio, which is very useful for electron transport and structural stability. Porous tubular structure has larger surface area than nanofibrous, and the holes on the surface can be conducive to the diffusion of gases. The ethanol-sensing properties of Ho-doped In$_2$O$_3$ PNTs sensor were investigated. This research shows that the structure of PNTs led to moderate improvements in the sensitivity of sensors. More than that, 6 mol% Ho-doped In$_2$O$_3$ PNTs sensors possess best gas-sensing properties (60 for 100 ppm) to ethanol. Their response value is higher than previous studies about ethanol sensor based on other In$_2$O$_3$ nanostructure. Not only that, the sensor also possesses fast response and recovery rate. These excellent

performances can be attributed not only to the porous structure and larger surface area of gas-sensing materials but also the catalysis of Ho dopant. The formation mechanism of the hollow or porous structure of Ho-doped In$_2$O$_3$ and the reasons for the improvement in ethanol-sensing properties were also discussed and analyzed in detail.

Experimental details

Materials

Polyvinylpyrrolidone-K90 (PVP-K90, 99.8%, M_w = 1,300,000) was purchased from Sigma–Aldrich (USA). In(NO$_3$)$_3$·4.5H$_2$O (99.9%), HoCl$_3$·6H$_2$O (99.9%), N,N-dimethylformamide (DMF, 99.5%) and C$_2$H$_5$OH (99.7%) were obtained from Aladdin (China). The above chemicals were of analytical grade and without further purification.

Synthesis

To synthesize the pristine and Ho-doped In$_2$O$_3$ PNTs, 0.2 g In(NO$_3$)$_3$·4.5H$_2$O was dissolved in mixed solvent comprised of 2 g DMF and 4 g ethanol with magnetic stirrers; an appropriate amount of HoCl$_3$·6H$_2$O was added to the above solvent. After stirring for 1 h, 0.3 g PVP was added to it. After further stirring for 6 h, homogeneous precursor solution was transferred into a plastic syringe with a metal spinneret that was connected to the positive electrode of a high-voltage power supply. A voltage of 18 kV direct current (DC) was applied between the cathode (a flat aluminum foil) and the anode (syringe tip), and the distance between the two electrodes was 25 cm. After a period of electrospinning, the as-collected nonwovens were placed into a muffle furnace and calcined (12 °C/min) in air at 550 and 600 °C for 2 h to form pure or Ho-doped In$_2$O$_3$ NTs and PNTs, respectively (Fig. 1a).

Fabrication and measurement of the gas sensors

In a typical fabrication procedure, first, the fabricated sample was blended with a tiny bit of deionized water to form a paste; the above paste was applied on the surface of a ceramic tube that was equipped with preinstalled a pair of Au electrodes and four Pt wires.

Figure 1 a Schematic diagram of synthesizing In$_2$O$_3$ NTs and PNTs and sensor device fabrication. **b** The experimental setup for testing gas sensitivity and the detection circuit.
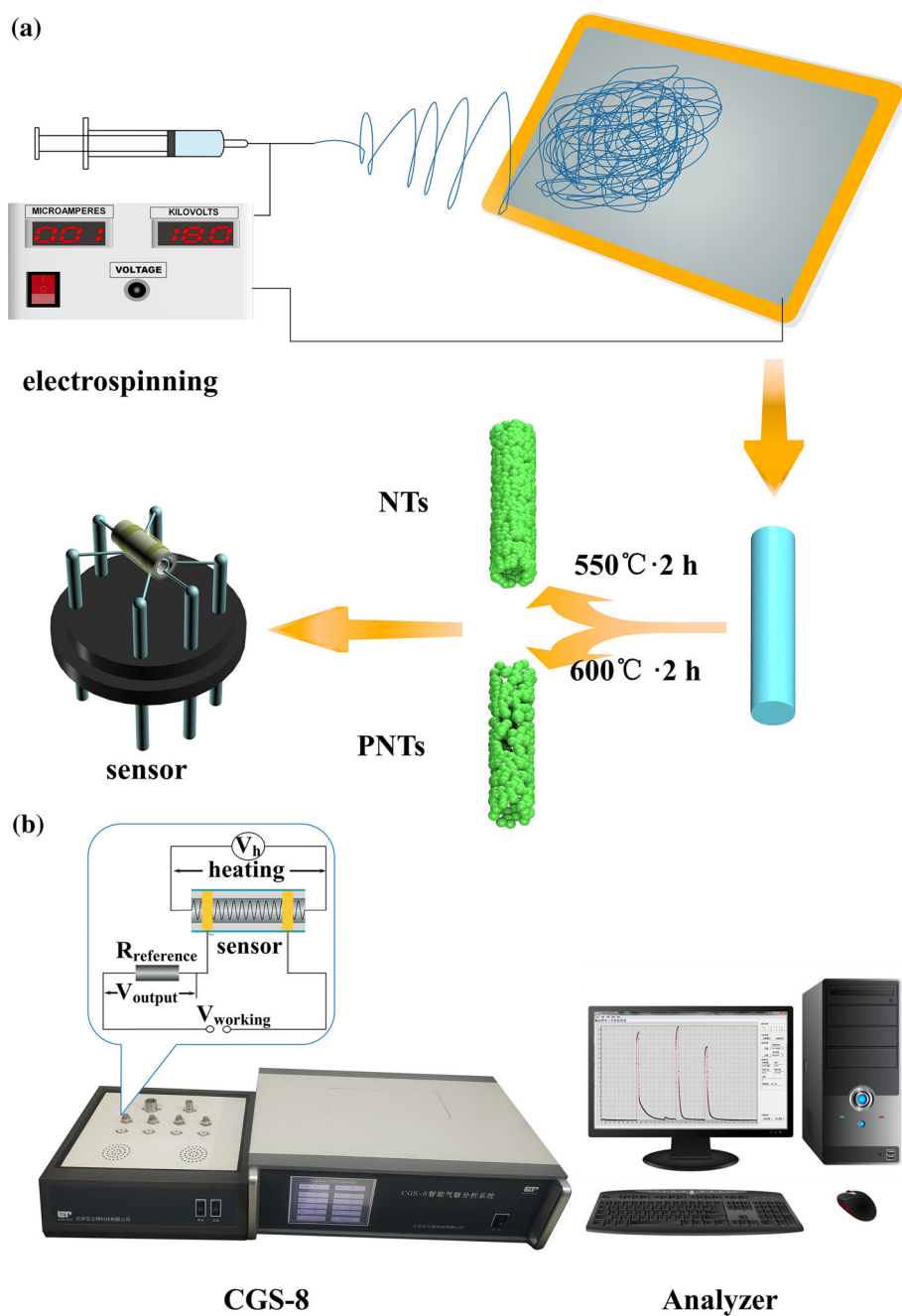
A Ni–Cr alloy heating silk was placed in the inner of alumina ceramic tube to offer the operating temperature for sensors. To obtain a good stability, the as-fabricated sensors were matured at 250 °C for at least 10 h before test.

For the gas concentration generated and controlled, static liquid gas distribution method has been used to obtain different gas volume fractions of the target volatile organic compound gases. The corresponding of liquid volume of VOCs and desired concentration of the test gas can be calculated by the following formula [18]:

$$V = \frac{V' \, CM}{22.4\rho} \tag{1}$$

where V (μL) is the injection volume, V' (L) is the test chamber volume, C (ppm) is the test gas concentration, M (g/mol) is the molecular weight of liquid and ρ (g/mL) is the density of the liquid.

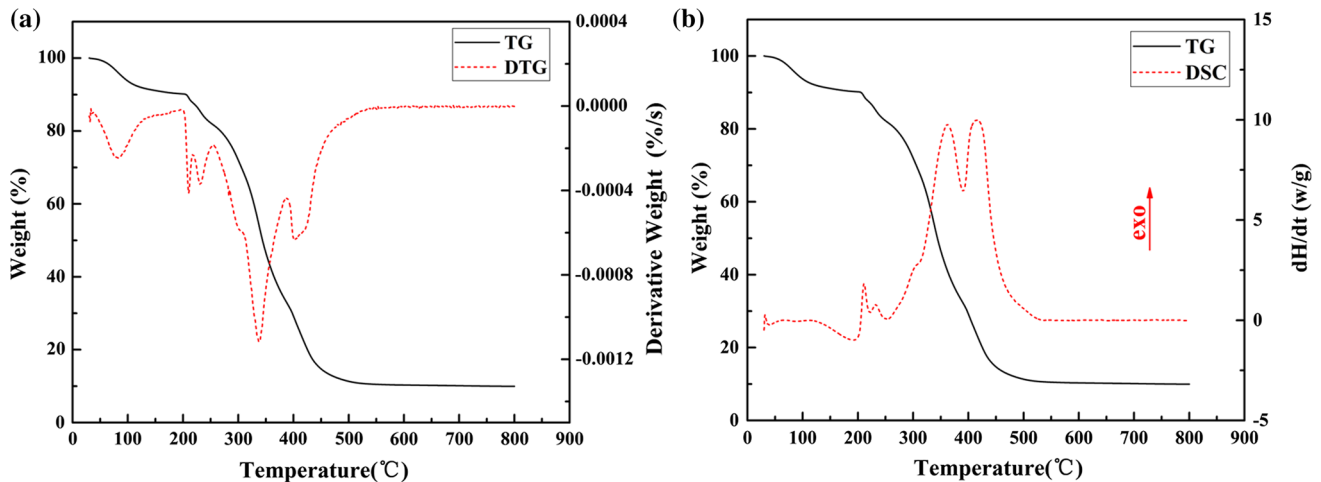For the gas-sensing study, change in electrical resistance of sensors as a function of time was

Figure 2 **a** TG/DTG and **b** TG/DSC curves of Ho-doped In_2O_3 nanofibers.

recorded through a CGS-8 gas sensitivity instrument that was coupled to the computer via a serial interface cable (Fig. 1b). The operating temperature of sensors could be controlled by adjusting the heating current. During the process of testing, the target gas or corresponding liquid whose volume is calculated according to Eq. (1) was injected into the test gas chamber (18 L) using syringe, and the electric fan was used to mix the target gas with ambient air. When the sensor resistance reached new constant value, the gas chamber was opened to recover the sensors in ambient air. The particular software that is designed for the instrument is provided to display real-time data and deal with the measuring data automatically.

The sensor response value (S) was defined as the ratio $S = R_a/R_g$, in which R_a was the resistance of sensor in air, and R_g was that in test gas. In addition, the response and recovery times were separately defined as the time taken by the sensor to achieve 90% of the overall resistance changes during adsorption and desorption process.

Characterization techniques

An XRD-6000 X-ray diffractometer (XRD, Shimadzu, Kyoto, Japan, with CuKα radiation, $k = 1.5406$ Å) was applied to research the crystal structures. Scanning electron microscopy (SEM) and energy-dispersive spectroscopy (EDS) analysis images of the samples were obtained using a scanning electronic microscopy (FEI Magellan 400 FEI Corp., Hillsboro, Oregon, US) and EDS attachment (OXFORD,

X-MAX150, UK). The transmission electron microscopy (TEM) images were recorded on a JEM-2200FS transmission electron microscope. Thermogravimetric/differential thermal analysis was performed using a TGA/DSC simultaneous thermal analyzer (Mettler-toledo TGA/DSC 3+, Greifensee, Switzerland) in air atmosphere. The Raman spectra of samples were taken at room temperature using Raman spectrometer (Renishaw inVia Microscope) with 488 nm excitation wavelength. The sensing properties were detected using a CGS-8 intelligent gas-sensing analysis system (Beijing Elite Tech, Beijing, China).

Results and discussion

TG/DTG and TG/DSC

Thermal properties of the pure In_2O_3 nanofibers are obtained from TG/DSC simultaneous analysis, in which heating rate is 10 °C min^{-1}. As shown in Fig. 2 a and b, the weight loss (ca. 10%) in the range of 30–200 °C can be attributed to the evaporation of absorbed water and residual solvent (ethanol and DMF), and the weight losses are more easily determined by integrating the peaks in the first derivative (DTG) curve. The simultaneously recorded DSC curve shows a wide endothermic peak. The two weight loss peaks from 200 to 255 °C is due to the removal of crystal water of the nitrates and the side chains of PVP, respectively, and the weight loss of this step is 8.74%. The sample weight is reduced to 33% of the initial value at 387 °C. Based on the DSC

curves, exothermic reactions due to the decomposition of some nitrate and the PVP backbone are shown at temperatures of approximately 300 and 350 °C. The decomposition temperature of pure PVP is about 380 °C according to the previous report [20], but the decomposition temperature of electrospinning nanofibers is declined by 30 °C. The emergence of this phenomenon is ascribed to lattice oxygen released by the decomposition of some nitrate and small size effect of nanofibers [21]. The last weight loss of 23% in the range of 387–550 °C is caused by oxycarbide generated by the PVP decomposition and the decomposition of the remaining nitrate. The DSC curve shows a big exothermic peak due to the above oxidation and the formation of In_2O_3 crystallization at 415 °C. These results indicate that the whole organic compounds are completely broken down to carbon dioxide before the temperature reached 550 °C. This is why 550 °C is selected as the initial annealing temperature.

XRD and EDS

Figure 3 shows the XRD patterns of pure In_2O_3 PNTs (sintering at 600 °C) and 6 mol% Ho-doped In_2O_3 nanofibers sintered at different temperatures. It can be observed that all the diffraction peaks are consistent with the cubic indium oxide (JCPDS card no. 06-0416). No additional peaks appeared, which indicates
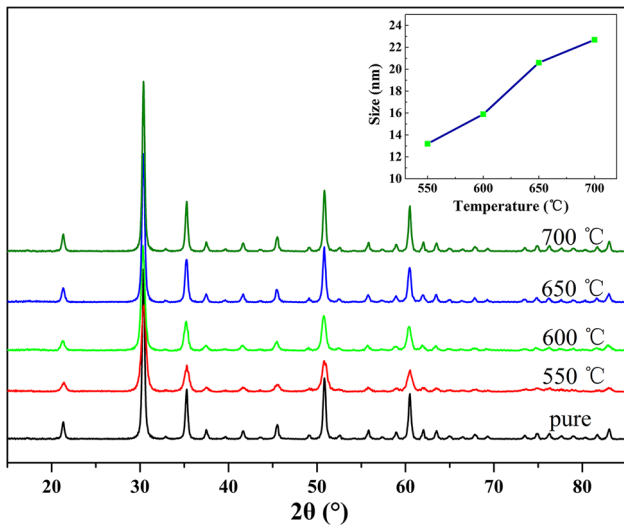
that the samples are purity. In addition, the peaks of Ho-doped In_2O_3 PNTs were slightly shifted to lower angle compared with pure In_2O_3 PNTs, which was due to the increased lattice spacing (the substitution of larger Ho^{3+} (0.894 Å) ions for In^{3+} (0.810 Å) [22]). The lattice parameters calculated from the XRD measurements of pure and 6 mol% Ho-doped In_2O_3 crystallite are 10.135 and 10.162 Å, respectively. The XRD patterns of 6 mol% Ho-doped In_2O_3 nanofibers heat-treated at different temperatures ranging from 550 to 700 °C are studied in more detail. It is obvious that the intensities of the peaks increase with the heat treatment temperature increases, which is mainly because of the growth of crystalline grain and the increase in crystallinity. And the grain size (d_m) is calculated using the XRD based on the Scherrer equation:

$$D = 0.89\lambda/\beta\cos\theta \tag{2}$$

where λ is the X-ray wavelength (1.5406 Å), θ is the Bragg diffraction angle and β on behalf of the peak width at half maximum. From the embedded figures, we can see that the crystal sizes for Ho-doped In_2O_3 PNTs increases with the increase in temperature. In addition, compared with the grain size of pure In_2O_3 PNTs (20.3 nm), the grain size of Ho-doped In_2O_3 PNTs (15.9 nm for 6 mol% Ho dopant) decreases in a certain extent.

Figure 4 displays the EDS pattern obtained from the Ho-doped In_2O_3 PNTs. It indicates that the
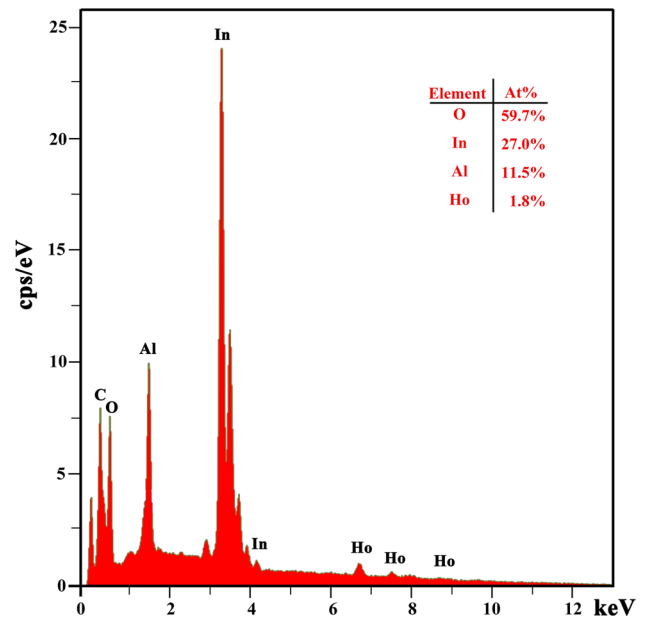

Figure 3 XRD patterns of pure In_2O_3 PNTs and 6 mol% Ho-doped In_2O_3 nanofibers sintered at different temperatures. The inset shows how that crystal sizes change as a function of temperature.

Figure 4 EDX pattern of 6 mol% Ho-doped In_2O_3 PNTs.

prepared materials are composed of In, O and Ho. The peak of C and Al is caused by conductive tapes and aluminum sample stage, respectively. The insert reveals the atoms percent of the sample under test, and the atoms percent of Ho element is almost consistent with actual mole fraction.

Raman spectra

Room-temperature Raman spectra were recorded in the spectral range of 250–700 cm^{-1} to investigate the defect states of pure In_2O_3 and Ho-doped In_2O_3 PNTs. Figure 5 displays the vibrational modes of all samples at 306, 366, 494 and 629 cm^{-1}, which are assigned to bcc-In_2O_3 [23, 24]. Especially for Ho-doped In_2O_3 PNTs, several notable features were observed. The intensity of the Raman peaks (306, 366, 494, 629 cm^{-1}) decreases with the increase in Ho^{3+} concentration, which may be due to loss of crystallinity and increase in structural disorder. The relative intensity of the peak at 366 cm^{-1}, with respect to maximum intensity peak at 306 cm^{-1}, is positively related to the presence of oxygen vacancies and increases with the Ho^{3+} content [25]. In other words, the number of oxygen vacancies will increase due to introducing Ho^{3+}.

SEM and HRTEM

Figure 6 shows typical SEM images of pure and Ho-doped In_2O_3 after different heat treatments. It was shown that the surface of In_2O_3 NTs with or without holes was controlled by calcination temperature. As
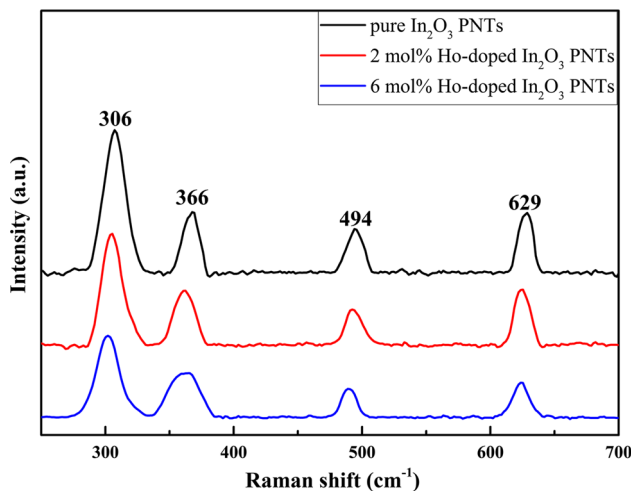
exhibited in Fig. 6a, after annealing to 550 °C for 2 h, well-defined In_2O_3 NTs are obtained. It can be clearly seen that the nanotube is homogeneous and leptodermous with diameters of nearly 100 nm. In contrast, it can be observed that the surfaces of the nanotubes were full of holes after calcination at 600 °C for 2 h (Fig. 3b). Meanwhile, Fig. 6c, d clearly demonstrates that the morphology of Ho-doped In_2O_3 is similar to the above. It follows that suitable amount of Ho element will not cause a great impact on the morphology of nanotube or porous nanotube. The morphology gradates from porous nanotubes to chain-like structure along with the increase in heat treatment temperature (Fig. 6e).

To further investigate the structure of the Ho-doped In_2O_3 sample, the HRTEM images of the nanostructured Ho-doped In_2O_3 heat-treated at 550 °C for 2 h are displayed in Fig. 6f. It shows that the interplanar spacings are 0.28 and 0.26 nm, attributed to the (1 0 0) and (0 0 2) planes of cubic bixbyite In_2O_3, respectively. The spotted ring-like SAED pattern shown in the insert of Fig. 6f further confirms the presence of cubic In_2O_3. The rings correspond to (211), (222), (400), (440), and (622) planes of In_2O_3. And the absence of any secondary phase in HRTEM images is in agreement with XRD data and indicates that Ho ions are diluted in In_2O_3 matrix.

The formation mechanism of nanotubes has been reported by many researchers [26–28]. Dayal and Kyu [26] reported that the development of diverse fiber morphologies depended on the match between the phase separation kinetics and the speed of solvent evaporation to some extent and that the nanotubes with uniform morphology are formed when the solvent evaporation process preponderates over the phase separation. Kirkendall diffusion effect plays an important role in the temporal evolution of the fiber morphology, according to other researchers [27, 28].

On the basis of the above-mentioned experiment and TG/DTG (Fig. 2), a possible formation mechanism of hollow nanofibers or porous In_2O_3 nanotubes was proposed based on the results of TGA and SEM as illustrated in Fig. 7. Firstly, for $In(NO_3)_3$/PVP composite nanofibers, $In(NO_3)_3$ and PVP are the main components, and during the electrospinning process, once nanofibers are spun out from the needle, most of ethanol and DMF will be vaporized. PVP functioned as a template for $In(NO_3)_3$. Secondly, during the calcination treatment, the $In(NO_3)_3$ situated near the surfaces of the nanofibers begin to decompose and

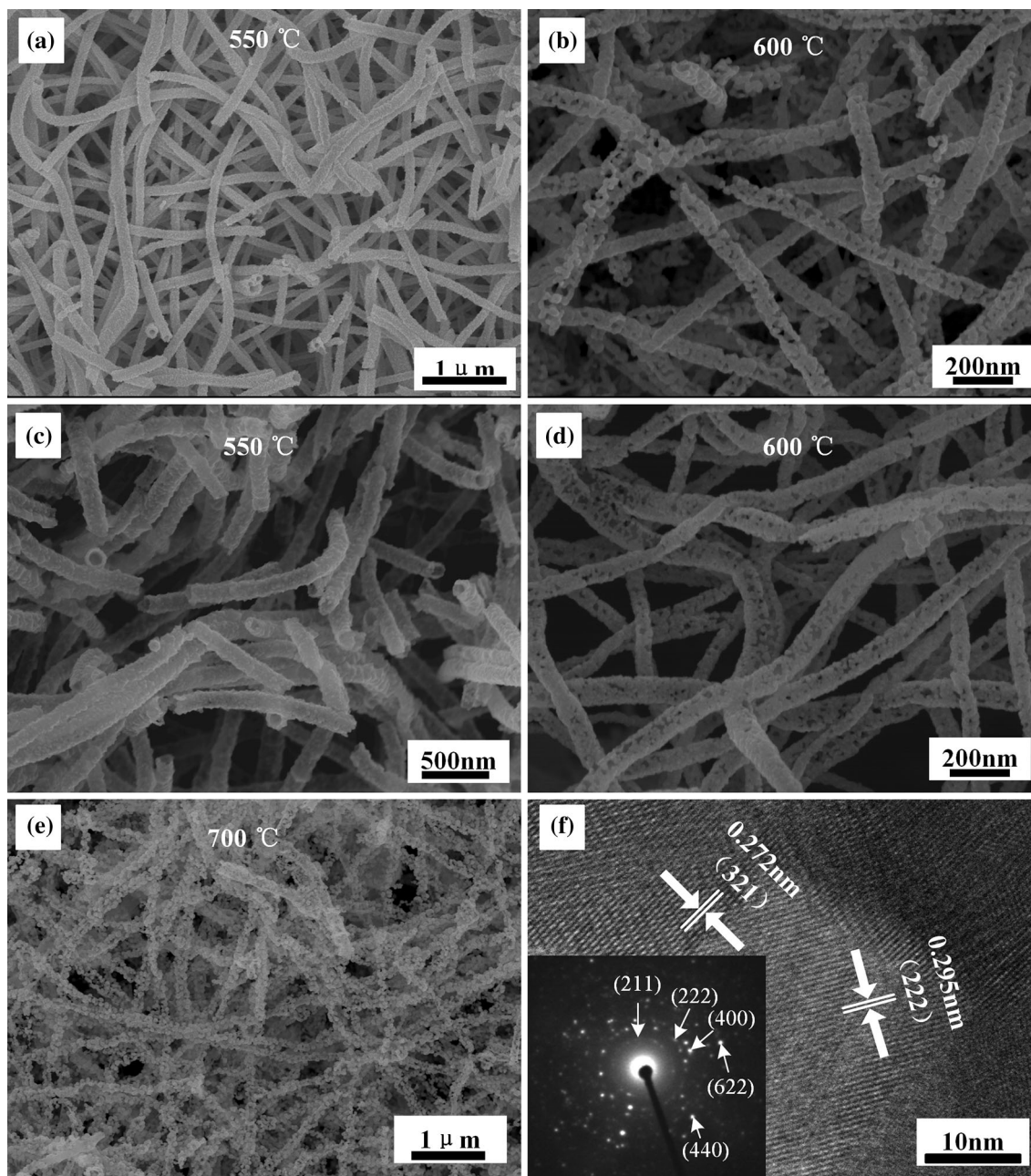**Figure 5** Raman shift of pure In_2O_3 and Ho-doped In_2O_3 PNTs.

Figure 6 SEM image of **a**, **b** pure and **c**–**e** Ho-doped In_2O_3 nanofibers calcined at different temperatures. **f** The HRTEM image and SAED of 6 mol% Ho-doped In_2O_3 PNTs.

form In_2O_3 particles (starting from about 220 °C). Simultaneously, it is difficult for the $In(NO_3)_3$ in the inside of the nanofibers to be oxidized, which is because of the lack of oxygen. In the meantime, the decomposition of PVP (side chains and partial backbone) happens when temperature increases (at about 255–390 °C). During the formation of In_2O_3 on the surface of nanowires, the inverse concentration gradients of $In(NO_3)_3$ and In_2O_3 particles in a radial

direction of the nanofibers impel $In(NO_3)_3$ to diffuse from the inside out and In_2O_3 particles from the outside in. However, the $In(NO_3)_3$ ($T_m = 100$ °C) melts much faster than the In_2O_3 particles ($T_m = 850$ °C). Therefore, vacancy diffusion is used to make up for the unbalanced movement of substances (Kirkendall effect) [27, 28]. This effect induces the formation of hollow structure near the inside (the side of faster diffusion). In addition, PVP as a
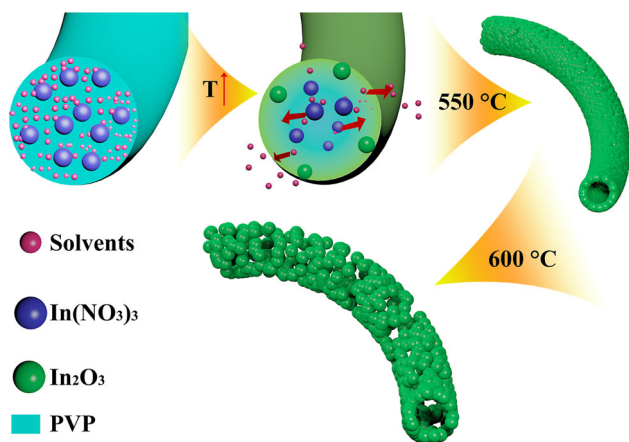
Figure 7 Possible formation mechanism of the In_2O_3 PNTs.

Figure 8 Response of pure In_2O_3 NTs (550 °C), pure In_2O_3 fractured PNTs (700 °C), pure and Ho-doped In_2O_3 PNTs (600 °C) (2, 4, 6 and 8 mol%) to 100 ppm ethanol at different operating temperatures.

removable template tries to break free from fibrous morphology control, whose gasiform oxide resultants (such as CO, CO_2) can prompt the outdiffusion of $In(NO_3)_3$. Finally, the PVP components will be decomposed completely at about 550 °C, and In_2O_3 NTs are obtained. For porous nanotubes, the heating temperature is higher. The In_2O_3 grain size increases with the further increase in temperature (the inset of Fig. 3b), which is possible because some smaller grain can combine to create larger one, and the inside of grain become more neat, the distance between particles become larger [29]. In addition, In_2O_3 grain may happen recrystal process during increasing temperature, and large grain become larger and small grain become smaller. Pores will be formed between larger grain and particles. So the pores appear equally over the entire surface of nanotubes.

Gas-sensing properties

The adsorption properties of the oxygen and response rates of target gases are temperature dependent [30], so most metal oxide gas sensors are also equipped with a heater that allows operation at a predetermined optimal operating temperature. Figure 8 shows the changes of response with operating temperature (from 200 to 270 °C) for the pure In_2O_3 NTs, pure and Ho-doped In_2O_3 PNTs (2, 4, 6 and 8 mol%) to 100 ppm ethanol. The response value of the sensor increases with the temperature increasing and goes for its peak at 240 °C and then decreases with a further increase in temperature. Therefore, 240 °C was the most appropriate operating temperature, so 240 °C was used in all the tests hereinafter. In addition, it can be obviously found that gas sensor

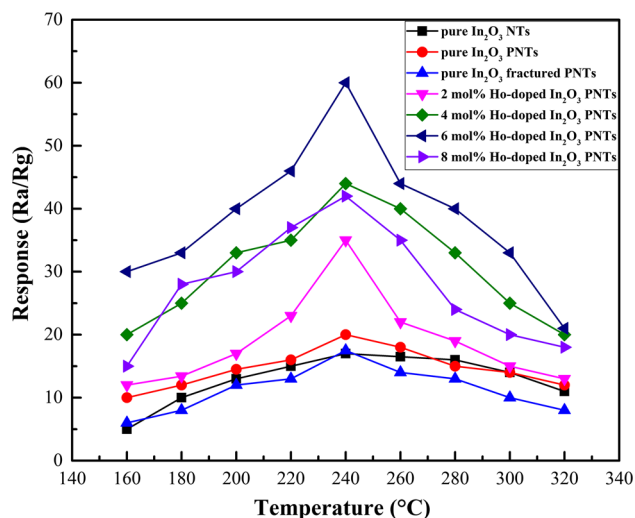based on porous structure displays better gas-sensing performance than sensor based on tubular construction. Moreover, the 6 mol% Ho-doped In_2O_3 PNTs demonstrated the highest sensitivity, and the pure In_2O_3-fractured PNTs (700 °C) show lower response than pure In_2O_3 PNTs (600 °C), and it is because that pure In_2O_3-fractured PNTs have lager grain size. From the above, we focus on 6 mol% Ho-doped In_2O_3 PNTs.

To clarify the influence of doping Ho element further, Fig. 9 shows the resistance and response transients of pure In_2O_3 NTs and PNTs sensors and 6 mol% Ho-doped In_2O_3 PNTs sensors exposed to 100 ppm ethanol at 240 °C. Figure 9a shows that Ho dopant can significantly increase the resistance of In_2O_3. As shown in Fig. 9b, pure In_2O_3 (response value is 17) takes on better gas sensitivity than pure In_2O_3 PNTs (response value is 20). Compared to pure In_2O_3 PNTs, the sensitivity of Ho-doped In_2O_3 PNTs (response value is 60) is triple. This may be because doping Ho element increases the number of effective sites (oxygen vacancies) of sensing materials [31, 32]. More specifically, the number of oxygen vacancies will increase due to the substitution of Ho for In, which will cause more electrons trapped by the increased oxygen vacancies in air [33]. When the sensor is exposed in air and in ethanol, it is obvious that the responses of the sensor change rapidly. The response and recovery time of the pure and 6 mol%
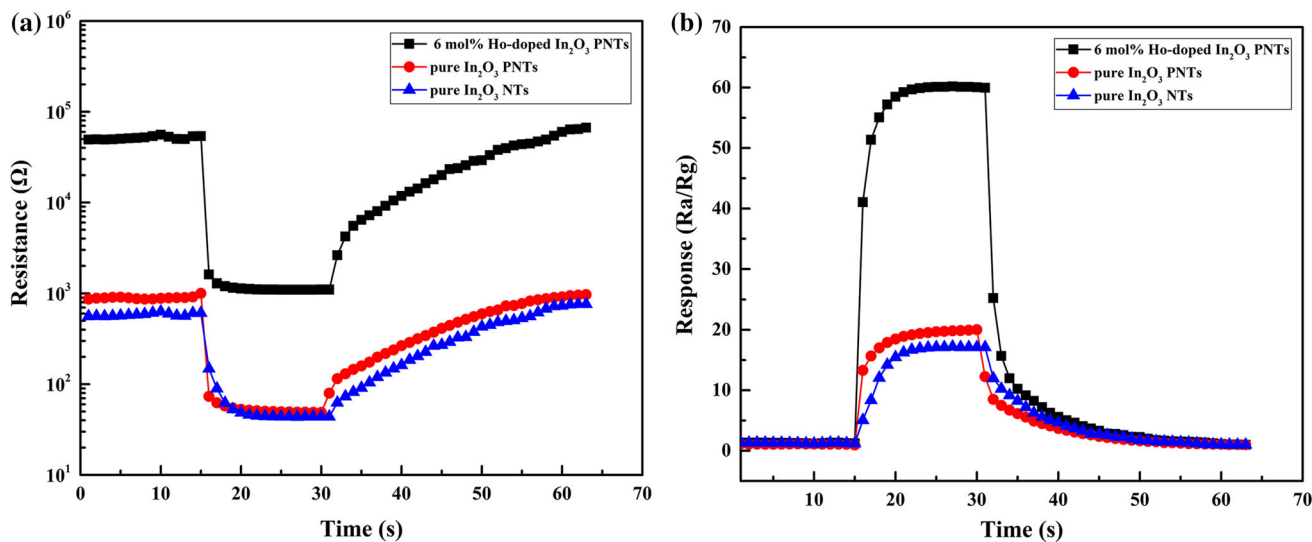
Figure 9 Dynamic resistance (**a**) and responses (**b**) of pure In_2O_3 NTs (550 °C) and PNTs (600 °C) sensors and 6 mol% Ho-doped In_2O_3 PNTs sensors versus 100 ppm ethanol concentration.

Ho-doped In_2O_3 PNTs are 5 and 30 s, 4 and 28 s, respectively. The rapid response and recovery performances can be attributed to the porous structure of the as-electrospun nanotubes, which can be more conducive to diffusion of ethanol molecules and improve the adsorption and desorption speed of target gas [34]. The above testify that Ho-doped In_2O_3 PNTs sensors have potential application.

The dependence of response value on ethanol concentration is measured and shown in Fig. 10. In the low concentration range (from 1 to 100 ppm), the response values is approximately linear with ethanol concentration. For clarity, the response of the sensors
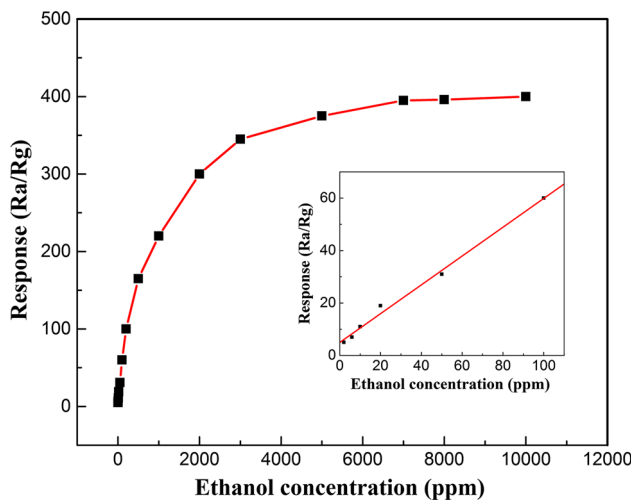

Figure 10 Response curves of Ho-doped In_2O_3 PNTs (600 °C) sensors to different concentrations of ethanol at 240 °C.

to lower concentration is shown in insert, and the limit of detection (LOD) was about 200 ppb. Above 100 ppm, the response value increases slowly with the ethanol concentration increasing, which indicates that the sensors become more or less saturated. The reason is that the sensors sensitivity is influenced by the number of effective sites [35]. However, the structure of porous nanotubes and crystals doped with Ho element has a pronounced effect on the amount of gas adsorption.

Selectivity is another important parameter for a sensing material in practical applications. As is evident in Fig. 11, selectivity histogram highlights the superior ethanol cross-sensitivity of Ho-doped In_2O_3 PNTs toward 100 ppm ethanol, acetone, formaldehyde, toluene, methanol, carbon monoxide, hydrogen and ammonia gases at 240 °C. It is well known that the selectivity of the sensor is influenced by several factors, such as the lowest unoccupied molecule orbit (LUMO) energy of the gas molecule and the amount of gas adsorption on the sensing material at different operating temperatures. Different gases have different energies of adsorption, desorption and reaction on the material surface [8, 40]. According to the previous reports, if the value of the LUMO energy of the gas molecule becomes smaller, the energy needed for the gas-sensing reaction will reduce and the sensing signal can be enhanced accordingly. Take ethanol and acetone for example, the values of the LUMO energy for ethanol and acetone are 0.12572 and 0.20525 eV, respectively, which means that the
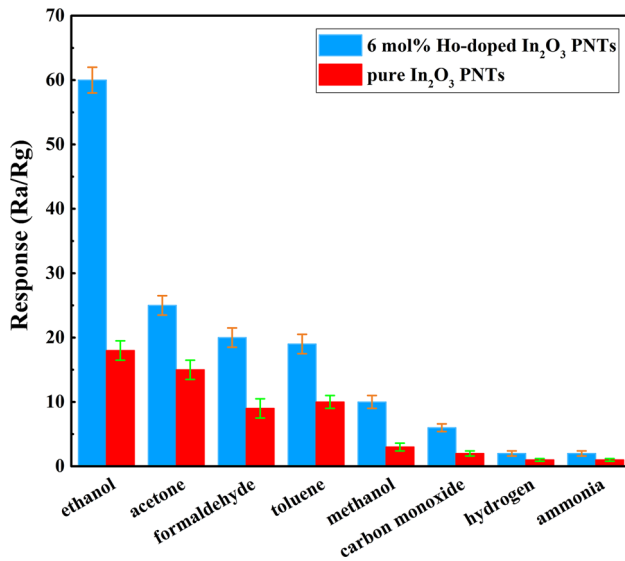
Figure 11 Responses of Ho-doped In_2O_3 PNTs (600 °C) sensors to different gases with a concentration of 100 ppm at 240 °C.

electrons transport more easily in ethanol molecules than in acetone molecules to the conductance band of Ho-doped In_2O_3 PNTs. Therefore, the Ho-doped In_2O_3 PNTs sensor shows higher sensitivity to ethanol than to acetone. Compared with the unconspicuous discrimination of pure In_2O_3 PNTs sensors to ethanol and acetone, the response of Ho-doped In_2O_3 PNTs sensors to ethanol is two and a half times different than that of acetone. The tested excellent sensitivity and selectivity of the 6 mol% Ho-doped In_2O_3 PNTs show that it is a suitable candidate for various practical application environments.
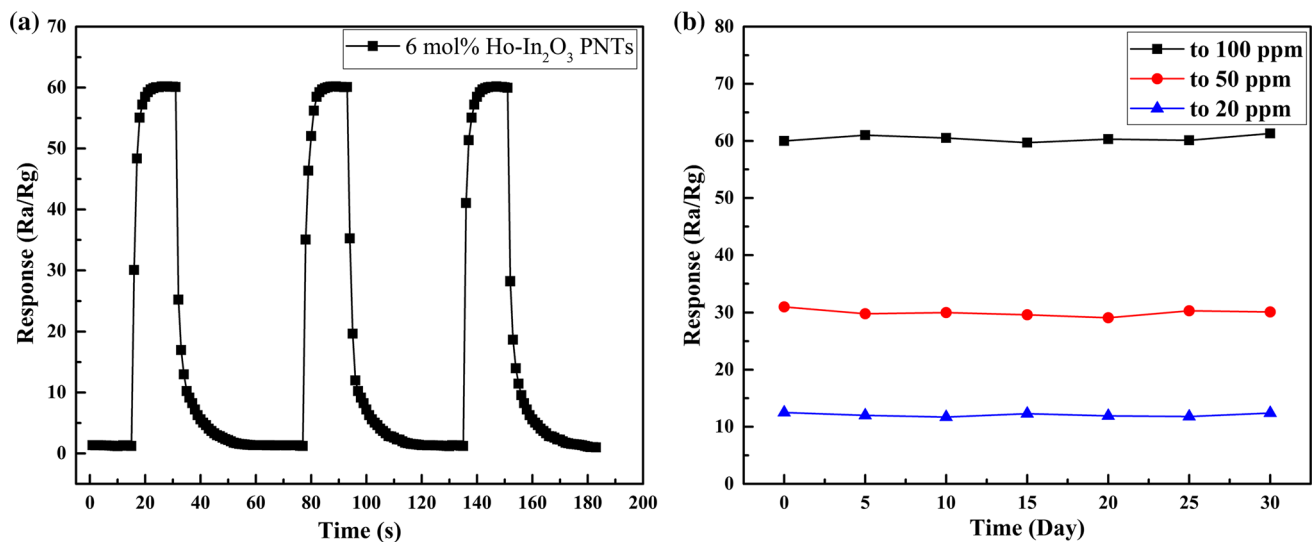
Figure 12a shows that the sensitivity value and response and recovery speed have almost unchanged during the three cycles, and the response value can recover about 1 after removing sensor from target gas to air. All the above behaviors confirmed the reproducibility and stability of Ho-doped In_2O_3 PNTs. Figure 12b displays the stability of Ho-doped In_2O_3 PNTs sensors to 20, 50 and 100 ppm ethanol at 240 °C within 30 days. It can be seen that the response of sensors basically have unchanged during the testing, demonstrating the good long-term stability of Ho-doped In_2O_3 PNTs.

Table 1 indicates that Ho-doped In_2O_3 nanotube sensors show a better sensitive to ethanol than other ethanol sensors using In_2O_3 as base-sensing material and noble metallic catalysts. Hence, the Ho-doped In_2O_3 nanotubes have potential to be used for ethanol sensor.

In general, for gas-sensing mechanisms of semiconducting metal oxides, the universally recognizable principle is the change of resistance when sensing materials is exposed to air or target gas [41]. Initially, when a sensor is placed in air, oxygen molecules are absorbed on the shell surface of Ho-doped In_2O_3 PNTs sensors and trap electrons from the conduction band of materials, which leads to the increase in resistance. After that, when ambient atmosphere rapidly goes from air to a reducing gas such as ethanol, oxygen radical anion will react with ethanol molecules and simultaneously release electrons back into the conduction band, and then, the resistance will drop. The following equations and

Figure 12 Reproducibility (**a**) and long-term stability (**b**) of Ho-doped In_2O_3 PNTs sensors.

Table 1 Comparison of response of ethanol sensors in the studies with the sensor based on Ho-doped In₂O₃ PNTs in this work

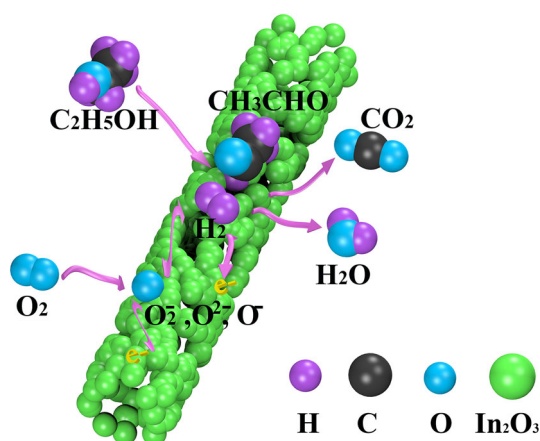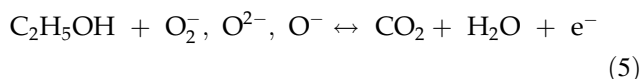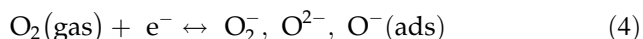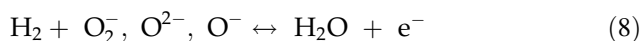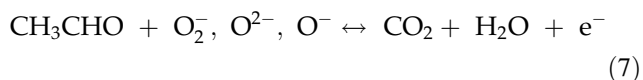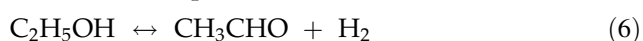| Materials and structure	T (°C)	C (ppm)	S (R_a/R_g)	References
In₂O₃/α-Fe₂O₃ nanotubes	225	100	21.4	[36]
Ga₂O₃–In₂O₃ nanocomposites	300	300	70	[37]
Dy-doped In₂O₃ nanoparticles	300	50	30	[38]
Pb-doped In₂O₃ nanostructures	250	100	33	[39]
Ho-doped In₂O₃ PNTs	240	100	60	This work

Figure 13 Schematic illustrating sensing mechanism of Ho-doped In₂O₃ PNTs (600 °C).

Fig. 13 are used to describe the reaction process [39, 42].

$$O_2(\text{gas}) \rightarrow O_2(\text{ads}) \tag{3}$$

$$O_2(\text{gas}) + e^- \leftrightarrow O_2^-, O^{2-}, O^-(\text{ads}) \tag{4}$$

$$C_2H_5OH + O_2^-, O^{2-}, O^- \leftrightarrow CO_2 + H_2O + e^- \tag{5}$$

Rare-earth oxides are basic oxides, and rare-earth doped semiconductor metal oxide has high surface basicity [43]. In fact, oxidation of ethanol on the surface of sensor undergoes dehydrogenation route [44]. Step reaction describes its dehydrogenation and oxidation as explained below:

$$C_2H_5OH \leftrightarrow CH_3CHO + H_2 \tag{6}$$

$$CH_3CHO + O_2^-, O^{2-}, O^- \leftrightarrow CO_2 + H_2O + e^- \tag{7}$$

$$H_2 + O_2^-, O^{2-}, O^- \leftrightarrow H_2O + e^- \tag{8}$$

In addition, it has been known to us that material with high specific surface area is more conducive to improve gas sensibility. For this experiment, the structure of hollow and porous can provide not only more bonding sites (oxygen vacancies) for absorbing more ethanol molecules, but also unhindered pathways which make gas molecules to easily penetrate to the whole porous nanotubes.

Simultaneously, the Ho element also provides vital role for improving the gas-sensing performances. It is generally known that In₂O₃ is an n-type semiconducting oxide because of oxygen vacancy [45]. When Ho element is doped into the In₂O₃, the inequality of ionic radius between Ho³⁺ (0.89 Å) and In³⁺ (0.81 Å) will give rise to the lattice deformation and imperfection, which will increase the number of oxygen vacancies [33, 38, 46]. To attain the stoichiometry of metal oxides, its oxygen vacancies will absorb atmospheric oxygen. It has been reported that oxygen vacancies can improve the binding interaction between gas molecules and metal oxide semiconductor nanotube [47]. In other words, the oxygen vacancies on the surface of In₂O₃ PNTs can server as electron donors, which is very beneficial for adsorbing oxygen molecules. In general, more electrons are trapped in air and released in ethanol atmosphere, which will lead to a higher response (more variation of resistance), when doping level is under 6 mol%. With the increase in Ho content, materials possess more active site for reacting with target gas [38]. However, when the doping level is higher than 6 mol%, the response value begins to decrease. This is because redundant Ho³⁺ will separate from the In₂O₃ crystal and form many clusters, reducing the electric transduction of In₂O₃ PNTs [48]. Furthermore, the ethanol molecules will be burned on the clusters surface without causing any electrical signal [49], so 6 mol% is the optimal doping ratio. In addition, the grain size of materials is another notable point [39, 42]. Ho dopant can effectively limit the grain growth of In₂O₃ according to XRD analysis, and the resistance of materials is significantly improved after doping Ho (Fig. 9a). According to Prabhu's research [50], the charge depletion layer of In₂O₃ (L) represented approximation by the Debye length (L_D) in air is about 10 nm at 240 °C and is

greater than $d_m/2$ (7.95 nm). And the whole grain will become depletion region in air, which shows a great change in resistance when sensors are moved from air to ethanol gas [42].

Conclusion

In summary, pure and Ho-doped In_2O_3 NTs and PNTs were successfully synthesized using a simple and cheap process, and the morphology of material was controlled simply by adjusting temperature. Their sensing properties of ethanol were investigated. This study has shown that in contrast to pure In_2O_3 NTs sensors, the sensors made out of pure In_2O_3 PNTs had higher response values, and in comparison with pure In_2O_3 PNTs sensors, In_2O_3 PNTs with an optimum Ho content level has gone a step further with response values, but the latter significantly outperformed the former for response values improvement, that is, 6 mol% Ho-doped In_2O_3 PNTs sensors exhibited the highest response (60 for 100 ppm). They also had short response/recovery time (4/28 s for 100 ppm) and excellent selectivity, and the lowest detection limit of ethanol was 200 ppb with the response value of 2. In the meantime, Kirkendall effect was used to explain the formation mechanism of nanotubes, and the presence or absence of pores on the surface of nanotubes was determined by calcination temperature. These advantages show that the Ho-doped In_2O_3 PNTs after heat treatment at 600 °C can be selected as a hopeful candidate for gas sensor in real-world usage.

Acknowledgements

References

[1] Guo L, Shen X, Zhu G, Chen K (2011) Sens Actuators B Chem 155:752. https://doi.org/10.1016/j.snb.2011.01.042

[2] Wagner T, Haffer S, Weinberger C, Klaus D, Tiemann M (2013) Chem Soc Rev 42:4036. https://doi.org/10.1039/C2CS35379B

[3] Katoch A, Abideen ZU, Kim J-H, Kim SS (2016) Sens Actuators B Chem 232:698. https://doi.org/10.1016/j.snb.2016.04.013

[4] Katoch A, Choi S-W, Kim SS (2014) Nanotechnology 25:455504. https://doi.org/10.1088/0957-4484/25/45/455504

[5] Espinosa EH, Ionescu R, Bittencourt C et al (2007) Thin Solid Films 515:8322. https://doi.org/10.1016/j.tsf.2007.03.017

[6] Kaniyoor A, Imran Jafri R, Arockiadoss T, Ramaprabhu S (2009) Nanoscale 1:382. https://doi.org/10.1039/b9nr00015a

[7] Qian LH, Wang K, Li Y, Fang HT, Lu QH, Ma XL (2006) Mater Chem Phys 100:82. https://doi.org/10.1016/j.matchemphys.2005.12.009

[8] Feng C, Li W, Li C et al (2012) Sens Actuators B Chem 166–167:83. https://doi.org/10.1016/j.snb.2011.12.083

[9] Okamoto A, Shibasaki I (2003) J Cryst Growth 251:560. https://doi.org/10.1016/S0022-0248(02)02448-X

[10] Bloor LG, Manzi J, Binions R et al (2012) Chem Mater 24:2864. https://doi.org/10.1021/cm300596c

[11] Chikhale LP, Patil JY, Rajgure AV, Shaikh FI, Mulla IS, Suryavanshi SS (2014) Ceram Int 40:2179. https://doi.org/10.1016/j.ceramint.2013.07.136

[12] Habibzadeh S, Khodadadi AA, Mortazavi Y (2010) Sens Actuators B Chem 144:131. https://doi.org/10.1016/j.snb.2009.10.047

[13] Qin W, Xu L, Song J, Xing R, Song H (2013) Sens Actuators B Chem 185:231. https://doi.org/10.1016/j.snb.2013.05.001

[14] Che G, Lakshmi BB, Martin CR, Fisher ER, Ruoff RS (1998) Chem Mater 10:260

[15] Tao X, Sun L, Li Z, Zhao Y (2009) Nanoscale Res Lett 5:383. https://doi.org/10.1007/s11671-009-9493-5

[16] Lakshmi BB, Patrissi CJ, Martin CR (1997) Chem Mater 9:2544. https://doi.org/10.1021/cm970268y

[17] Xu L, Song H, Dong B, Wang Y, Chen J, Bai X (2010) Inorg Chem 49:10590. https://doi.org/10.1021/ic101602a

[18] Xu L, Dong B, Wang Y, Bai X, Liu Q, Song H (2010) Sens Actuators B Chem 147:531. https://doi.org/10.1016/j.snb.2010.04.003

[19] Huang Z-M, Zhang YZ, Kotaki M, Ramakrishna S (2003) Compos Sci Technol 63:2223. https://doi.org/10.1016/S0266-3538(03)00178-7

[20] Azhari SJ, Diab MA (1998) Polym Degrad Stab 60:253. https://doi.org/10.1016/S0141-3910(97)00073-6

[21] Chen W-S, Huang D-A, Chen H-C et al (2009) Cryst Growth Des 9:4070. https://doi.org/10.1021/cg900297q

[22] Enhanced acetone sensing properties of Eu-In_2O_3 nanotubes with bumps (2016) Institution of Engineering and Technology, http://digital-library.theiet.org/content/journals/10.1049/mnl.2016.0235

[23] Kumar M, Singh VN, Singh F, Lakshmi KV, Mehta BR, Singh JP (2008) Appl Phys Lett 92:171907. https://doi.org/10.1063/1.2910501

[24] Olivia MB, Ariano DR, Cleocir JD, Alexandre JCL, Edson RL, Adenilson JC (2010) J Phys D Appl Phys 43:045401

[25] Gan J, Lu X, Wu J et al (2013) Sci Rep 3:1021. https://doi.org/10.1038/srep01021

[26] Dayal P, Kyu T (2006) J Appl Phys 100:043512

[27] Cho JS, Kang YC (2015) Small 11:4673

[28] Tu KN, Gösele U (2005) Appl Phys Lett 86:093111

[29] Yanping L, Zhihong L, Yuhu L, Zhiyong L, Qihou L (2014) Chin J Nonferrous Metals 24:221

[30] Shaalan NM, Rashad M, Abdel-Rahim MA (2016) Mater Sci Semicond Process 56:260. https://doi.org/10.1016/j.mssp.2016.09.007

[31] Lim SK, Hwang S-H, Chang D, Kim S (2010) Sens Actuators B Chem 149:28. https://doi.org/10.1016/j.snb.2010.06.039

[32] Gao L, Cheng Z, Xiang Q, Zhang Y, Xu J (2015) Sens Actuators B Chem 208:436. https://doi.org/10.1016/j.snb.2014.11.053

[33] Zhang L-h, Wang S-l, Liu F-h (2015) J Electron Mater 44:3408. https://doi.org/10.1007/s11664-015-3905-3

[34] Guo X, Zhang J, Ni M, Liu L, Lian H, Wang H (2016) J Mater Sci Mater Electron 27:11262. https://doi.org/10.1007/s10854-016-5247-1

[35] Yu F, Wu Y, Ma J, Zhang C (2013) J Environ Sci 25:195. https://doi.org/10.1016/S1001-0742(12)60023-0

[36] Zhao C, Zhang G, Han W et al (2013) Cryst Eng Commun 15:6491. https://doi.org/10.1039/C3CE40962G

[37] Bagheri M, Khodadadi AA, Mahjoub AR, Mortazavi Y (2015) Sens Actuators B Chem 220:590. https://doi.org/10.1016/j.snb.2015.06.007

[38] Anand K, Kaur J, Singh RC, Thangaraj R (2017) Chem Phys Lett 670:37. https://doi.org/10.1016/j.cplett.2016.12.057

[39] Montazeri A, Jamali-Sheini F (2017) Sens Actuators B Chem 242:778. https://doi.org/10.1016/j.snb.2016.09.181

[40] Navale ST, Bandgar DK, Nalage SR et al (2013) Ceram Int 39:6453. https://doi.org/10.1016/j.ceramint.2013.01.074

[41] Sun P, Cai Y, Du S et al (2013) Sens Actuators B Chem 182:336. https://doi.org/10.1016/j.snb.2013.03.019

[42] Franke ME, Koplin TJ, Simon U (2006) Small 2:36. https://doi.org/10.1002/smll.200500261

[43] Singh S, Singh A, Yadav BC, Dwivedi PK (2013) Sens Actuators B Chem 177:730. https://doi.org/10.1016/j.snb.2012.11.096

[44] Hamedani NF, Mahjoub AR, Khodadadi AA, Mortazavi Y (2012) Sens Actuators B Chem 169:67. https://doi.org/10.1016/j.snb.2012.02.074

[45] Miller DR, Akbar SA, Morris PA (2014) Sens Actuators B Chem 204:250. https://doi.org/10.1016/j.snb.2014.07.074

[46] Anand K, Kaur J, Singh RC, Thangaraj R (2016) Ceram Int 42:10957. https://doi.org/10.1016/j.ceramint.2016.03.233

[47] An W, Wu X, Zeng XC (2008) J Phys Chem C 112:5747. https://doi.org/10.1021/jp711105d

[48] Cheng JP, Wang BB, Zhao MG, Liu F, Zhang XB (2014) Sens Actuators B Chem 190:78. https://doi.org/10.1016/j.snb.2013.08.098

[49] Belmonte JC, Manzano J, Arbiol J et al (2006) Sens Actuators B Chem 114:881. https://doi.org/10.1016/j.snb.2005.08.007

[50] Prabhu E, Gnanasekar KI, Ravindran TR, Jayaraman V, Gnanasekaran T (2014) J Electrochem Soc 161:B176. https://doi.org/10.1149/2.0451409jes